University of Groningen

Highly tunable magnetic spirals and electric polarization in Gd0.5Dy0.5MnO3

De, Chandan; Bag, Rabindranath; Singh, Surjeet; Orlandi, Fabio; Manuel, Pascal; Langridge, Sean; Sanyal, Milan K.; Rao, C. N. R.; Mostovoy, Maxim; Sundaresan, A.

IMPORTANT NOTE: You are advised to consult the publisher's version (publisher's PDF) if you wish to cite from it. Please check the document version below.

Document Version
Publisher's PDF, also known as Version of record

[Link to publication in University of Groningen/UMCG research database](link)

Highly tunable magnetic spirals and electric polarization in Gd$_{0.5}$Dy$_{0.5}$MnO$_3$

Chandan De,[1] Rabindranath Bag,[2] Surjeet Singh,[2] Fabio Orlandi,[3] Pascal Manuel,[3] Sean Langridge,[3]
Milan K. Sanyal,[1,4] C. N. R. Rao,[1] Maxim Mostovoy,[5] and A. Sundaresan[1]

[1]*School of Advanced Materials, Chemistry and Physics of Materials Unit, Jawaharlal Nehru Centre for Advanced Scientific Research, Jakkur P.O., Bangalore 560064 India*
[2]*Indian Institute of Science Education and Research, Pashan, Pune 411008, India*
[3]*ISIS Facility, STFC Rutherford Appleton Laboratory, Chilton, Didcot, Oxfordshire, OX11 0QX, United Kingdom*
[4]*Saha Institute of Nuclear Physics, Bidhannagar, Kolkatta 700064, India*
[5]*Zernike Institute for Advanced Materials, University of Groningen, Nijenborgh 4, Groningen 9747 AG, The Netherlands*

Recent progress in the field of multiferroics led to the discovery of many new materials in which ferroelectricity is induced by cycloidal spiral orders. The direction of the electric polarization is typically constrained by spin anisotropies and magnetic field. Here, we report that the mixed rare-earth manganite, Gd$_{0.5}$Dy$_{0.5}$MnO$_3$, exhibits a spontaneous electric polarization along a general direction in the crystallographic *ac* plane, which is suppressed below 10 K but reemerges in an applied magnetic field. Neutron-diffraction measurements show that the polarization direction results from a large tilt of the spiral plane with respect to the crystallographic axes and that the suppression of ferroelectricity is caused by the transformation of a cycloidal spiral into a helical one, a unique property of this rare-earth manganite. The freedom in the orientation of the spiral plane allows for a fine magnetic control of ferroelectricity, i.e., a rotation as well as a strong enhancement of the polarization depending on the magnetic-field direction. We show that this unusual behavior originates from the coupling between the transition-metal and rare-earth magnetic subsystems.

I. INTRODUCTION

There has been a resurgence of interest in multiferroic materials showing the simultaneous presence of magnetic and ferroelectric orders, with a promising cross-linking between them, which is an important parameter for applications such as magnetoelectric memory, spintronics, sensors, and magneto-electric microwave devices [1–10]. Coexisting magnetic- and electric dipole orders are often found in frustrated magnets where the electric polarization is induced by unconventional spin orders breaking inversion symmetry of the crystal lattice [7–9]. Frustrated magnetism leads to many competing states and complex phase diagrams. In orthorhombic rare-earth (*R*) manganites *R*MnO$_3$ (*R* = Dy, Tb, and Gd), ferroelectricity is associated with the cycloidal spiral ordering of the Mn spins [1,2,11,12]. The electric polarization vector lies in the spiral plane and is perpendicular to the spiral wave vector in accordance with the inverse Dzyaloshinskii-Moriya mechanism and the spin current model of the magnetically induced ferroelectricity [13–15]. The orientation of the spiral plane depends on the ionic size of *R* ion and applied magnetic fields [16]. For example, *R*MnO$_3$ with *R* = Tb and Dy shows the cycloidal spiral state with the wave vector along the *b* axis and spins lying in the *bc* plane which induces a polarization, P_c, in the *c* direction [17,18]. In an applied magnetic field along the *b* axis, the polarization vector reorients from the *c*- to the *a* direction due to a flop of spiral spins from the *bc* to the *ab* plane, in which the magnetic point groups change from $mm21'$ to $2mm1'$ [11]. GdMnO$_3$ is close to the borderline separating the nonpolar collinear *A*-type antiferromagnetic (AFM) state from the polar noncollinear spiral states [11]. Its precise location in the phase diagram remains a controversy and the nature of various competing phases is not well understood. Magnetization and single-crystal synchrotron x-ray data suggest that below 23 K the Mn spins order in the *A*-type AFM state which is weakly ferromagnetic and paraelectric [19,20]. This is inconsistent with a small electric polarization observed in a narrow temperature interval around the Gd ordering temperature (∼6.5 K) [11,12]. Moreover, magnetic field applied along the *b* axis induces a ferroelectric state below 23 K with the electric polarization, P_a, comparable to that in Tb and Dy compounds. In this state, both the Mn and Gd spins show a commensurate spin ordering along the *b* axis [19,20]. The field-induced ferroelectricity is believed to originate from a commensurate *ab* cycloidal spiral [20,21]. Indeed, in a related compound, Gd$_{0.7}$Tb$_{0.3}$MnO$_3$, the *ab* spiral state with the polarization parallel to the *a* axis was observed in neutron-diffraction studies [22].

In addition to the strong effect of the size of the rare-earth ions on competing exchange interactions between Mn^{3+} spins and thus the magnetic structure and dielectric properties of rare-earth manganites, the coupling between the *R*-ion and Mn^{3+} magnetic subsystems also plays an important role. In the case of TbMnO$_3$, the electric polarization mainly comes from the Mn-magnetic subsystem. On the other hand, in DyMnO$_3$, an incommensurate magnetic ordering of Dy ions, which is induced by the spiral ordering of Mn spins and has the same wave vector, gives a significant contribution to the total electric polarization. This is evident from the large polarization drop below the commensurate magnetic ordering of Dy spins ($T_N^{Dy} = 7$ K) when the rare-earth ions no longer

contribute to the electric polarization and only the polarization induced by Mn spins remains [23]. These facts prompted a number of systematic studies of orthorhombic manganites with mixed R ions [24,25], which revealed rich phase diagrams resulting from competition of collinear, noncollinear, commensurate, and incommensurate magnetic phases that can coexist in spatially uniform and phase-separated states. Nonetheless, multiferroic properties of manganites near the phase boundary between the ab and bc cycloidal phases as well as effects of the interplay between the Mn- and R magnetic orders are not well understood. An earlier study on polycrystalline $R_{0.5}Dy_{0.5}MnO_3$ (R = Eu, Gd) showed an unusual behavior of electric polarization and its enhancement under magnetic field [26].

In this work, we report magnetic and dielectric properties of $Gd_{0.5}Dy_{0.5}MnO_3$ (hereafter referred to as GDMO) single crystals along with a neutron-diffraction study on polycrystalline ^{160}Gd-enriched GDMO. The ferroelectric state of this material shows polarization both along the a and c axes, which is consistent with the fact that the cycloidal plane lies $\sim 40°$ from the ab plane, as revealed by neutron diffraction. Intriguingly, the appearance of short-range magnetic ordering of R ions suppresses the ferroelectric cycloidal state of Mn^{3+} spins and induces a helical spin structure with a small cycloidal component that results in a weak but finite electric polarization. The peculiar spin structure of GDMO allows for a fine control of the polarization direction in the ac plane that is not observed in any of the known $RMnO_3$ compounds. We will discuss this complex temperature and field behavior in terms of the magnetic symmetry and of the Mn- and R-spins contributions.

II. EXPERIMENTAL

Single crystals were grown by the floating-zone method and the phase purity of the grown crystal was confirmed by powder-x-ray-diffraction technique (Bruker D8 Advance). For this purpose, small pieces were cut from the crystal boule and ground into fine powders. Crystal homogeneity was confirmed by optical microscopy under polarized light and scanning electron microscopy (Zeiss Ultra Plus, Germany). Three platelike samples cut along the principal axes [100], [010], and [001] with a dimension of about 2 mm × 2 mm × 0.3 mm were used for measurements. Neutron-diffraction measurements were made on polycrystalline sample containing ^{160}Gd isotope on the high-resolution powder diffractometer "WISH" at ISIS, United Kingdom [27]. The JANA2006 software was used to perform the Rietveld refinements of the neutron data whereas group theoretical calculations were carried out with the help of the ISODISTORT software [28,29]. Magnetic measurements were performed in a vibrating-sample magnetometer superconducting quantum interference device. Heat capacity was measured in Physical Property Measurement System (PPMS). Dielectric constant measurement was performed using Agilent E4980A Precision LCR meter. Pyrocurrent was measured using Keithley electrometer (6517A). Both the electrical measurements were performed in PPMS which provided the required temperature and magnetic field. For the pyroelectric current measurement, the sample was cooled across the transition temperature with applied electric field. At the low temperature the electrodes were shorted. After about

30 min, the electrometer was connected to the sample and the current was measured while heating the sample with 4 K/min rate without applying any electric field. For the dc-bias current measurement, the sample was cooled down to the lowest temperature without an electric poling and the current is recorded while warming the sample in the presence of an electric field [30]. This procedure enables one to obtain both the polarization and depolarization currents in a single measurement at the transition temperature which is shown schematically in Supplemental Material, Fig. S15 [31]. This technique has already been applied in several multiferroic studies [32–34].

III. RESULTS

A. Magnetic phase transitions

Figures 1(a) and 1(b) show the temperature dependence of the heat capacity divided by temperature, C/T, and magnetization, $M(T)$, along the three crystallographic axes of a single-crystal sample of GDMO. Heat capacity data show three anomalies that can be associated with the collinear incommensurate ordering ($T_{N1}^{Mn} = 39.5$ K), cycloidal ordering ($T_{N2}^{Mn} = 16.5$ K) of Mn spins, and ordering of R ions at $T_N^R = 5$ K, similar to the magnetic transitions observed in Tb and Dy manganites [1]. Magnetic susceptibility, dominated by rare-earth spins, shows a cusp at T_N^R [Fig. 1(b)] corresponding to a broad peak in C/T. The large suppression of the heat capacity peak at T_N^R under a magnetic field $H_b = 8$ T and the nature of $M(H)$ data[inset of Fig. 1(b)] indicates the metamagnetic nature of R-ion ordering [see Supplemental Material, Figs. S1–S4 for $M(H)$, dM/dH, $M_T(H)$] [31]. On the other hand, the anomaly at T_{N2}^{Mn} becomes more prominent, increasing by 3 K at $H_b = 8$ T.

B. Temperature-dependent spontaneous electric polarization

First, we discuss the unusual behavior of the spontaneous electric polarization in the temperature range 2–30 K, measured after an electric poling (5.6 kV/cm) from 30 to 2 K. Figures 1(c) and 1(d) show the development of a spontaneous polarization both along the a and c directions (P_a and P_c), respectively, below the cycloidal ordering temperature, which is consistent with the anomaly in the dielectric permittivities, ε_a and ε_c, as shown in the respective figures. The observation of polarization along the a and c directions, in the single-crystal specimens, indicates that the spontaneous polarization has a general direction in the ac plane. Intriguingly, the polarization P_a drops sharply at low temperatures from 1200 $\mu C/m^2$ at 7 K to a remnant polarization of $\sim 100 \mu C/m^2$ at 2 K, while P_c drops from 200 to 100 $\mu C/m^2$ in the same temperature interval. The decrease of electric polarization below 7 K indicates that the magnetic ordering of R ions triggers a transition of the Mn magnetic subsystem into a nonferroelectric (or a weakly ferroelectric) state. The presence of dielectric anomaly in both ε_a and ε_c at 5 K indicates that the low-temperature state is a polar phase (see Fig. S5) [31]. The suppression of the ferroelectric spiral ordering of Mn spins by the R magnetic ordering is unique to this compound. It may be mentioned here that the suppression of polarization reported in $Gd_{0.7}Tb_{0.3}MnO_3$ is due to a transition from cycloidal to nonpolar A-type antiferromagnetic phase [22].
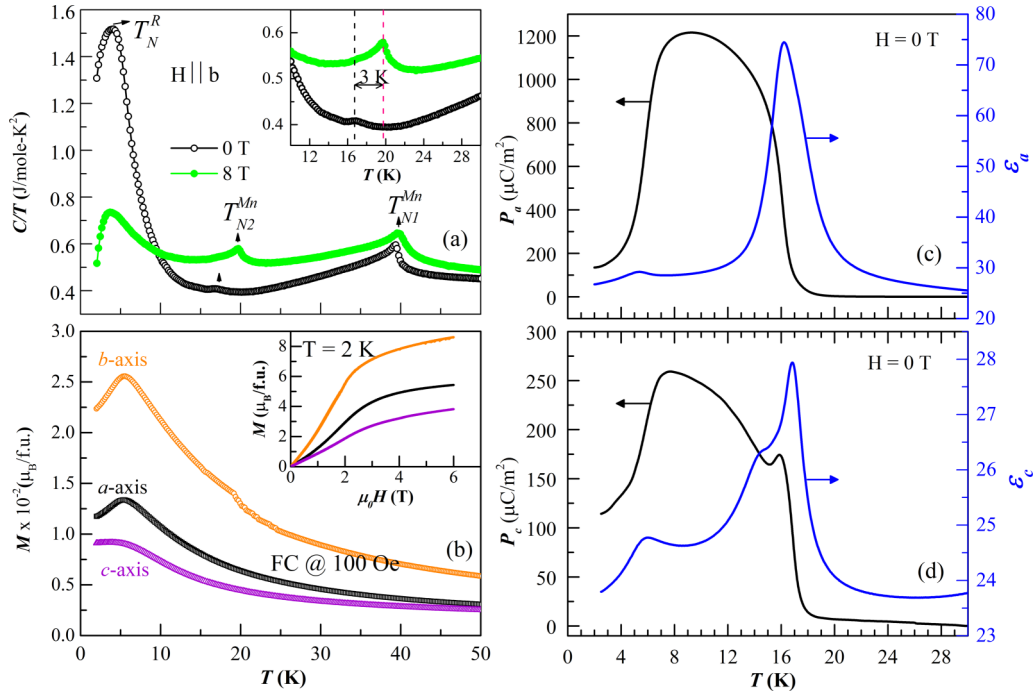
FIG. 1. Temperature dependence of heat capacity and magnetization. (a), (b) Heat capacity divided by temperature and magnetization as a function of temperature, respectively. Three anomalies corresponding to the Mn spin-density wave, Mn cycloidal and R-ion ordering at T_{N1}^{Mn}, T_{N2}^{Mn}, and T_{N}^{RE} can be clearly seen. (c), (d) Electric polarization P_a and P_c and ε_a and ε_c versus temperature, respectively.

C. Effect of magnetic field on the polarization (P_a and P_c)

In the magnetic field applied along the a direction, P_a is suppressed while P_c increases along with the recovery of

the low-temperature polarization [Figs. 2(a) and 2(b)]. As in DyMnO$_3$, ε_a and ε_c show high sensitivity to the applied magnetic field near the flop transition [see insets of Fig. 2(a) and
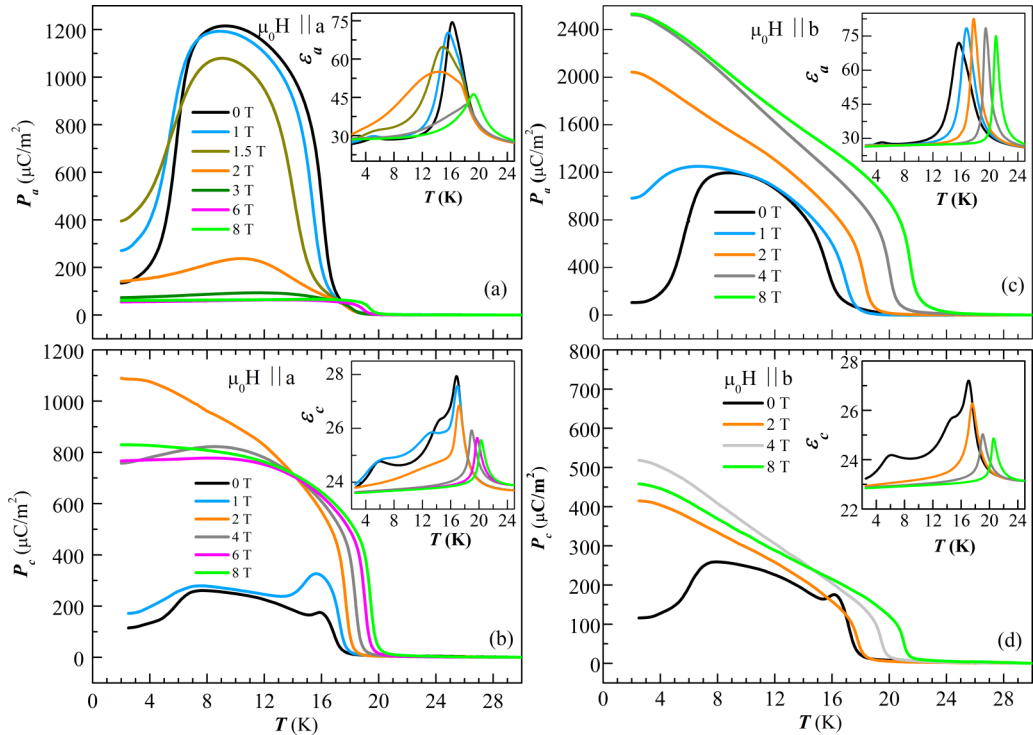

FIG. 2. Temperature dependence of electric polarization. (a), (b) Suppression and enhancement of the electric polarization of P_a and P_c when magnetic field is applied along the a direction. (c), (d) Temperature dependence of P_a and P_c under applied field along the b direction. Insets show the corresponding dielectric data.

2(b)], the so-called giant magnetocapacitance effect [2]. The ferroelectric Curie temperature increases by about 4 K under the magnetic field of 8 T. When the magnetic field is applied along the *b* axis, both the Curie temperature and polarization (P_a and P_c) increase monotonously with H_b [Figs. 2(c) and 2(d)]. At $H_b = 8$ T and 2 K, $P_a = 2500\,\mu\text{C m}^{-2}$, which is 25 times larger than the zero-field value and is comparable to the polarization in the *ab* spiral state of DyMnO$_3$ [11]. While H_b in TbMnO$_3$ and DyMnO$_3$ induces the flop transition from the *bc*-spiral to the *ab* spiral state [2,11], no flop transition is found in GDMO; remarkably, the polarization along the *c* axis, P_c, also increases: at $H_b = 8$ T it is five times larger than in zero field [Fig. 2(c)]. The behavior observed in H_c is similar to that in H_b, except that the growth of P_a is less dramatic [see Fig. S6 for P_a, P_c ($H \parallel c$)] [31]. Furthermore, P_a has a maximum around 3 T and decreases upon further increase of the magnetic field. The polarization along the *b* direction is shown in Fig. S7 [31].

D. Neutron-diffraction results in polycrystalline ^{160}Gd-substituted GDMO

In order to understand the unusual temperature and magnetic field dependence of the spontaneous polarization, we have carried out neutron-powder-diffraction studies of ^{160}Gd-substituted GDMO. The refinement of the nuclear structure within the *Pbnm*1′ space group returns good agreement factors between the observed and calculated data as shown by the Rietveld plots in Fig. S8 [31]. The refinement of the average occupancy of the *A* site is in agreement with the nominal composition and details of the nuclear refinement are reported in Supplemental Material (Tables S1 and S2) [31]. Below $T_{\text{N1}}^{\text{Mn}} = 39.5$ K a set of reflections, ascribable to magnetic ordering of the Mn sublattice, is observed and indexed with a propagation vector $\mathbf{k} = (0\,0.308(4)\,0)$. An attempt to refine the observed diffraction pattern with a spin-density wave (SDW) aligned with one of the unit-cell directions gives poor results. For this reason the SDW axis was allowed to rotate in the *ab* plane and a good agreement with the data (Fig. S9 [31]) was obtained with the moment approximately aligned along the [120] direction with an amplitude of 2.83(9) μ_B at 25 K (see Fig. S10 [31]). The magnetic ordering is described by a nonpolar space group, point group $2/m1'$ (a detailed description of the symmetry analysis is reported in Supplemental Material, Tables S3 and S4 [31]), in agreement with the polarization measurements. Upon crossing $T_{\text{N2}}^{\text{Mn}}$, a strong and abrupt increase of the magnetic intensity indicates a change in the spin configuration as also suggested by the pyrocurrent measurements and heat capacity data. It should be emphasized that we do not observe the appearance of new magnetic reflections and that all the measured satellites can be indexed with a single propagation vector $\mathbf{k} = (0\,0.309(4)\,0)$. This evidence combined with the observation of sharp magnetic reflections and a spontaneous electrical polarization in the *ac* plane in single-crystal specimens suggests the presence of a single magnetic phase. As in the other *R*MnO$_3$ compounds [1], this transition is related to the appearance of a cycloidal spin structure. The refined magnetic structure is schematically shown in Figs. 3(a)–3(c) [31] and consists of a cycloidal spiral in the (102) plane with an ordered moment of 2.80(9) μ_B at
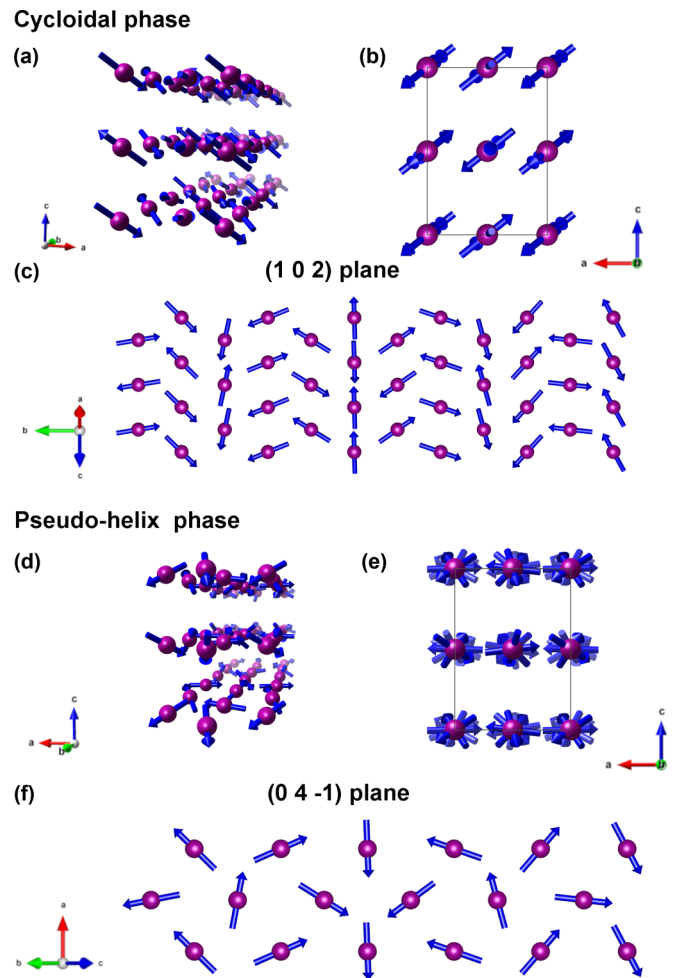

FIG. 3. Magnetic ordering of the different incommensurate phases of GDMO. Magnetic structures of the cycloidal phase (a), (b), and (c) and for the *p*-helix phase (d), (e), and (f) in different projections [31]. (a) A 3D view of the cycloidal phase. (b) Projection of the cycloidal structure in the *ac* plane showing the spins in the (102) plane. (c) Projection along the [102] direction showing the rotation of the cycloidal structure in the (102) plane. (d) A 3D view of the *p*-helix phase. (e) Projection of the *p*-helix structure in the *ac* plane showing the perpendicular component to *k*. (f) Projection along the [041] direction showing the rotation of the Mn spins in the (041) plane. In all panels are reported the axes directions referring to the crystal structure (red *a* axis, green *b* axis, and blue *c* axis). Mcif files of the refined magnetic structures are available as Supplemental Material [31].

11 K; for a detailed symmetry description see Supplemental Material, Tables S5 and S6 [31]. The tilting of the manganese cycloidal plane by ∼40° from the *ab* plane is allowed by the magnetic point group $m1'$ and it is in agreement with the observation of a spontaneous polarization in both the *a* and *c* directions. Moreover, assuming equal magnetoelectric coupling constants along the *a* and *c* directions, the induced polarization should be parallel to the [20–1] direction, in agreement with the hierarchy of the measured polarization along *a* and *c*, with $P_a > P_c$. The magnetic superspace group, $Pn1'(0\beta0)0s$ (see Tables S5 and S6 for details [31]), actually allows the cycloidal plane to freely rotate around the *b* axis

without symmetry breaking. This can explain the change of the polarization from P_a to P_c, above T_N^R, when magnetic field is applied along the a direction. Interestingly, the value of the propagation vector along the b direction remains unchanged between the spin-density wave and the cycloidal phases, in contrast with the other orthorhombic rare-earth manganites.

Below 10 K a clear rise of diffuse scattering in the diffraction data is observed (see Fig. S12), indicating the setting of short-range correlations. From the intensity of the diffuse scattering, heat capacity, and magnetization measurements [see Figs. 1(a) and 2(b)] it is possible to conclude that below T_N^R a short-range ordering of the rare-earth moments develops. Moreover a set of satellite reflections is observed, which can be indexed with the same propagation vector as the cycloidal structure. In particular, the observation of the $000 + k$ and $110 - k$ magnetic reflections, absent in the cycloidal phase, suggests the presence of a sizable magnetic component perpendicular to the propagation vector direction characteristic of a helical phase. The best refinement of the neutron data at base temperature is obtained within the same space group of the cycloidal phase (see Fig. S13 [31]) and the resulting magnetic structure is drawn in Figs. 3(d)–3(f). The structure is characterized by a spiral spin arrangement with the spin rotating in the (041) and (04–1) planes alternating along the c axis [see Figs. 3(e) and 3(f)], with an ordered moment of $3.17(11)\,\mu_B$. This spiral structure can be decomposed into a large nonpolar helical component perpendicular to the propagation vector direction and a smaller polar cycloidal component. The magnetic structure and the point group $m1'$

are consistent with the pyrocurrent measurements indicating a strong decrease of the spontaneous polarization but still a finite value of P_a and P_c. The finite value of the electrical polarization is due to the "cycloidal" part of the magnetic structure induced through the spin-current mechanism [13–15], whereas the large helical component perpendicular to the propagation vector is nonpolar since the parent space group (*Pbnm*) is not a ferroaxial group [35]. Owing to the larger helical component we will call this phase pseudohelix (*p* helix) below. It is worth stressing that the *p*-helix phase is still described in the same superspace group as the cycloidal one, since the magnetic symmetry does not constrain the phase relations between the different sinusoidal components, meaning that the phase transition between the two phases can occur with a continuous rotation or with a sudden jump of the cycloidal plane in an isostructural phase transition. Unfortunately, our diffraction data combined with the fact that the two phases have the same propagation vector do not allow discriminating between the two cases. Figure 4 (left) shows the integrated intensity versus temperature of some magnetic reflections characteristic of each phase, highlighting the different transitions temperatures. It is interesting to note that the intensity of the $110 - k$ and $000 + k$ reflections, characteristic of the *p*-helix phase, increases below T_{N2}^{Mn} following an almost linear dependence typical of a secondary (induced) order parameter. It is, therefore, likely that the rotation of the cycloidal plane from the (102) plane to the (041)/(04–1) is induced from the short-range ordering of the *R*-ion moments on the *A* sites.
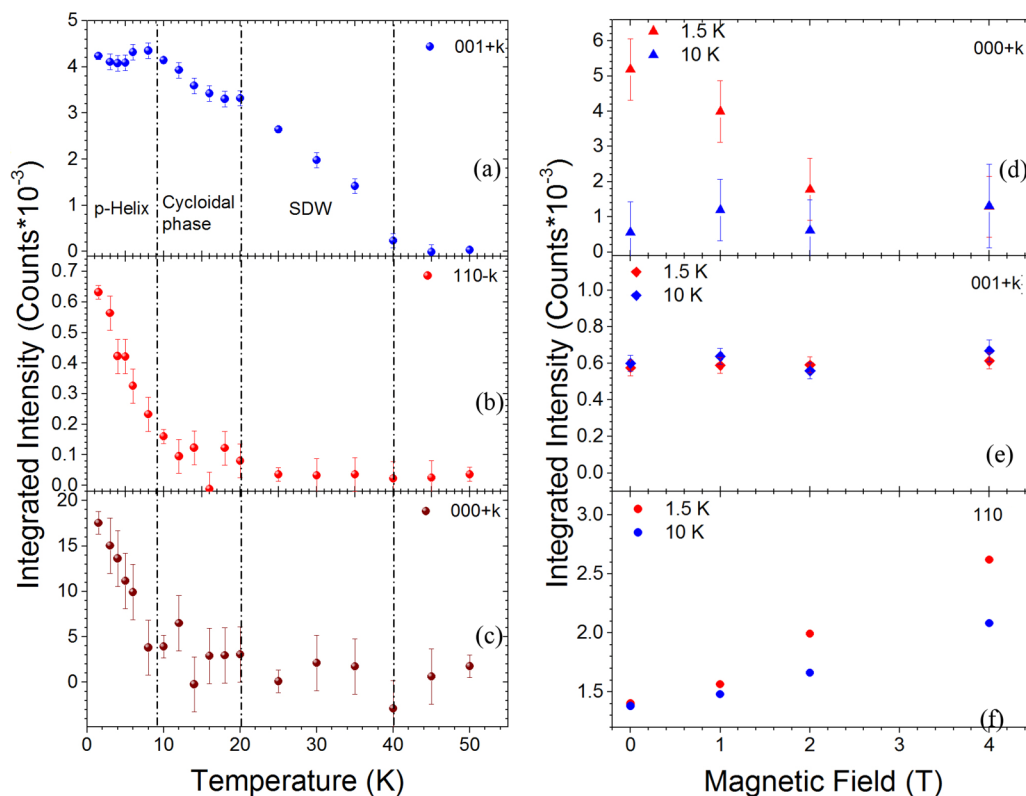

FIG. 4. Integrated intensity of magnetic reflections characteristic of each magnetic phase as function of temperature (a), (b), (c) and applied magnetic field (d), (e), (f).

In order to study the role of the R-ions short-range ordering on the Mn spin and the strong increase in the electric polarization in the p-helix phase under external magnetic field, a series of in-field powder-neutron-diffraction experiments were performed. The increase of the applied magnetic field induces a clear decrease of the diffuse scattering with a concomitant increase of the diffracted intensity on some nuclear reflections as shown in Fig. S14 [31]. These magnetic contributions, with the $k = 0$ propagation vector, are ascribable to a ferromagnetic polarization of the R ion as also observed in the macroscopic magnetization measurements [Fig. 1(b)]. As shown in Fig. 4, from the integrated intensity of the 110 reflection, the ferromagnetic polarization of the R ions can be obtained both above and below T_N^R. More interesting is the effect of the applied field on the Mn sublattice ordering. Figure 4 (right) shows the integrated intensity of the $000 + k$ and $001 + k$ satellite reflections, characteristic of the p-helix and cycloidal phase, respectively, versus the applied field above and below T_N^R. It clearly demonstrates that the application of an external magnetic field below T_N^R induces the transition from the p-helix phase to the cycloidal one as indicated by vanishing $000 + k$ satellite reflection, explaining also the strong increase of the polarization along the a and c axes. In contrast, the application of the magnetic field above the short-range ordering of the R ions does not change the cycloidal plane of the Mn spins, as shown by the integrated intensity of the magnetic satellites at 11 K (Fig. 4).

E. Electric polarization in the *p*-helix phase

The relatively small remnant polarization ($\sim 100 \, \mu C/m^2$) is associated with the p-helix state. The presence of such a small polarization is demonstrated by our detailed pyroelectric current measurements as discussed below. The first evidence comes from pyrocurrent measurements with different poling intervals [Fig. 5(a)]. For the poling intervals 8–2 K and 7–2 K, we see negative (T_{N2}^{Mn}) and positive (T_N^R) pyrocurrent peaks corresponding to the appearance and disappearance of Mn polarization, respectively, similar to those observed for 30–2 K poling interval [inset in Fig. 2(c)], except that the pyrocurrent values are smaller because the poling is done well below the Curie temperature. On the other hand, for the poling interval 6.5–2 K, we observe only a negative peak at T_N^R. This negative peak is not related to the disappearance of Mn polarization but indicates a polar state associated with the helical ordering. In order to further explore the polar nature of the low-temperature phase, we have measured pyrocurrent under various magnetic fields for the same poling interval. Figure 5(b) shows the suppression of the low-temperature polarization by magnetic field related to changes in the R-spin structure, which correlates with the metamagnetic behavior shown in Fig. S1 [31]. The small negative pyrocurrent peaks at T_{N2}^{Mn} in Fig. 5(b), corresponding to the Mn spiral ordering, are induced by the depolarization current at T_N^R. At $H_a = 8$ T, the low-temperature polar phase disappears and so does the peak at T_{N2}^{Mn}. It can be noted here that the polarization obtained by
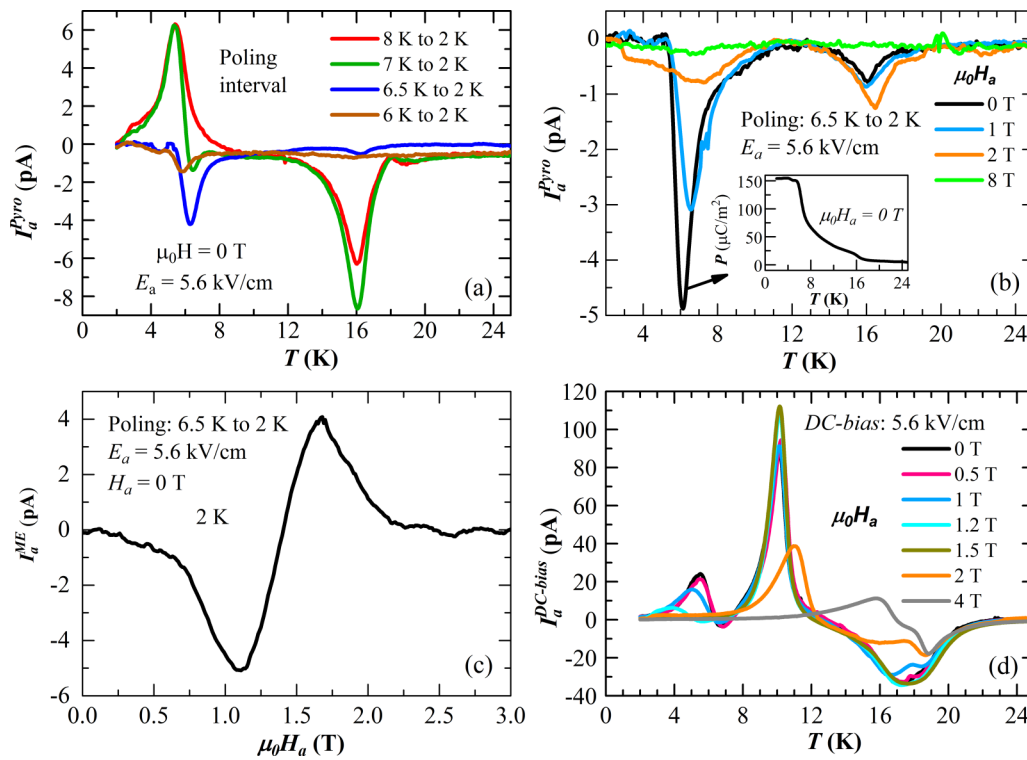

FIG. 5. Pyrocurrent, magnetoelectric current, and dc-bias current. (a) Pyrocurrent data recorded along the a axis for different poling intervals between 8 and 2 K with 5.6 kV/cm. A negative peak appears at the rare-earth ordering when the poling field is applied from 6.5 to 2 K. (b) Pyrocurrent measured along the a axis under various H_a after poling from 6.5 to 2 K. Inset shows polarization along the a axis in zero magnetic field poled between 6.5 and 2 K. (c) Magnetoelectric current recorded at 2 K while ramping the field from 0 to 3 T after poling the sample from 6.5 to 2 K with 5.6 kV/cm in zero magnetic field. (d) dc-bias current measured along the a axis with 5.6 kV/cm at various magnetic fields along the a axis.
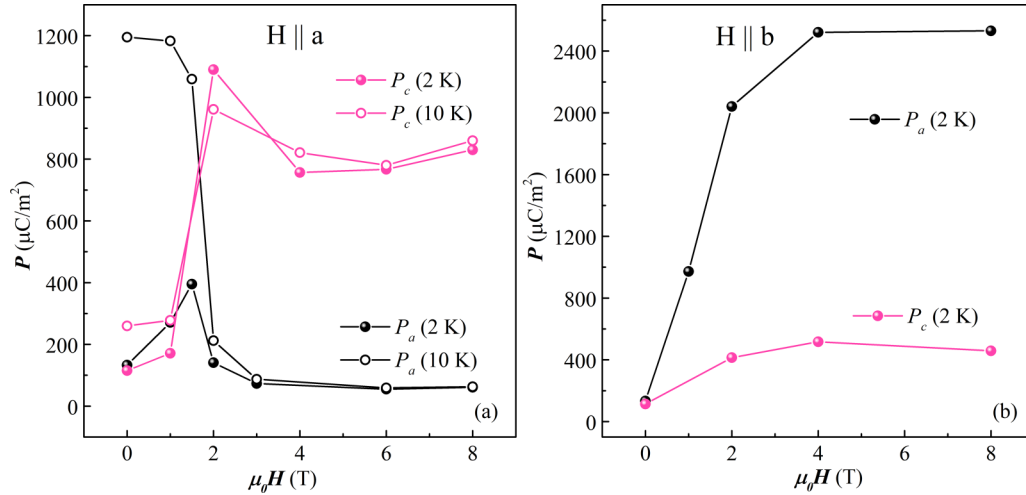
FIG. 6. Magnetic field dependence of electric polarization. (a) Change of P_a and P_c under an applied field along the a direction and (b) Enhancement of polarization P_a and P_c under $H \parallel b$.

integrating the pyrocurrent in zero field [inset of Fig. 5(b)] is comparable to the remnant polarization at 2 K (Fig. 2). The ferroelectric nature of the low-temperature state ($T < T_N^R$) is further supported by the magnetic field dependence of the current measured at 2 K [Fig. 5(c)] showing a negative peak at ∼1.1 T and a positive peak at ∼1.5 T. These peaks correspond to the disappearance of the low-temperature polarization and appearance of the spiral-induced polarization, respectively.

To further confirm the presence of small polarization in the low-temperature state, we have employed the dc bias current measurement [30]. In our measurement, the sample was cooled down to 2 K and the current I_a was recorded in the presence of an applied electric field (5.6 kV/cm) while warming in various magnetic fields ($H \parallel a$) [Fig. 5(d)]. In zero field, we observe a positive peak at 6 K followed by a small negative peak near 7 K, corresponding to the polarization and depolarization currents, respectively, which confirms the independent origin of ferroelectric order in the low-temperature state and is consistent with the dielectric anomaly at T_N^R [Figs. 1(c) and 1(d) and Supplemental Material, Fig. S5)]. Similarly, we observe the polarization and depolarization currents due to the spiral ordering of Mn spins at 10.5 and 17 K, respectively. Under magnetic field, we see that the low-temperature polarization peaks are suppressed and only the peaks associated with the Mn spiral ordering remain.

IV. DISCUSSION

We summarize the temperature- and magnetic field dependence of polarization in Fig. 6. For magnetic field applied along the a direction, P_a and P_c at 10 K clearly demonstrate the switching of polarization direction from $P_a > P_c$ to $P_c > P_a$ related to rotation of the cycloidal plane towards the bc plane. At 2 K, P_a is small because the cycloidal component in the p-helical ground state is small. The application of the field at 2 K induces the transition to the cycloidal phase, by destroying the short-range AFM ordering of the R ion, which will be in the same orientation at 10 K and hence with P_c big and P_a small. P_c follows switching behavior at 10 K from $P_a \sim P_c$ to $P_c > P_a$. On the other hand, P_a under $H \parallel b$ shows

a gigantic enhancement, reaching a value ($2500\,\mu C/m^2$) comparable to the maximum polarization reported for $DyMnO_3$. A schematic phase diagram is provided in Fig. 7 in order to show the various magnetic phases as function of applied field and temperature.

Theoretical model

As the nature of the short-range rare-earth magnetic order is unknown, we focus on Mn spin degrees of freedom, which we describe by the Landau free-energy expansion in powers of the A-type antiferromagnetic order parameter (ferromagnetic ab layers coupled antiferromagnetically along the c axis), $\mathbf{A} = (A_a, A_b, A_c)$ [36]:

$$f = \frac{c}{2}\mathbf{A}\left(\frac{d^2}{dy^2} + Q^2\right)^2\mathbf{A} + \frac{a}{2}A^2 + \frac{b}{4}A^4 + f_{ani}, \quad (1)$$

where $a = \alpha(T - T_0)$ and $f_{ani} = \frac{1}{2}\delta a_a A_a^2 + \frac{1}{2}\delta a_c A_c^2 + \frac{1}{2}b_{ac}A_a^2 A_c^2 + \frac{1}{2}b'_{ac}(A_a\frac{dA_c}{dy})^2$ is the anisotropy energy in which
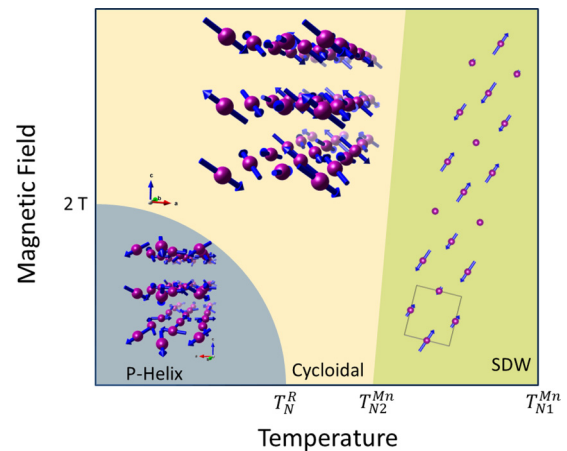

FIG. 7. Experimental phase diagram of the GDMO system. Schematic phase diagram of various magnetic phases with temperature and magnetic field.
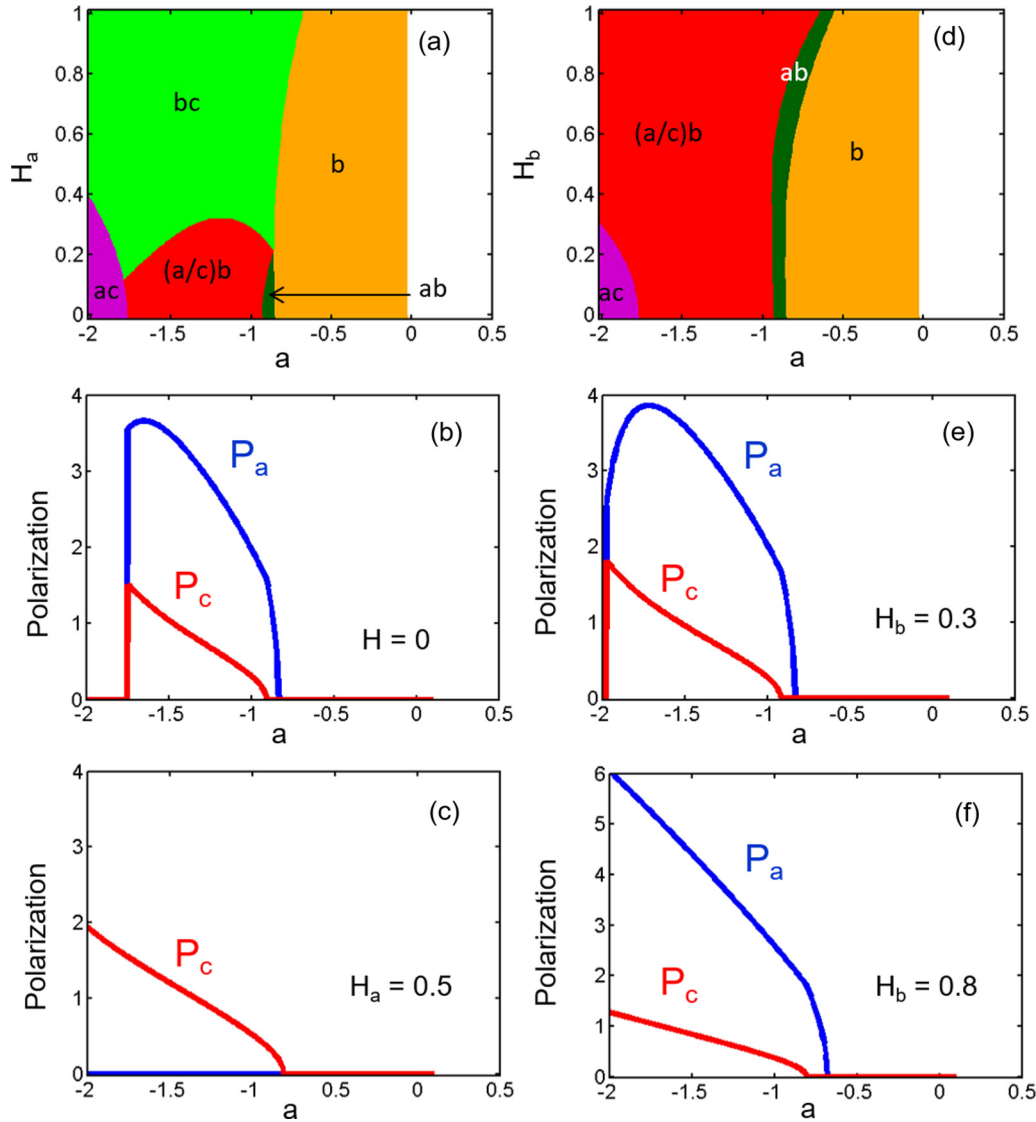
FIG. 8. Phase diagrams and magnetic field dependence of the electric polarization for the model (1). Phase diagrams for $H \parallel a$ (a) and $H \parallel b$ (d) showing the regions of the paramagnetic (white), incommensurate collinear with spins parallel to the b axis (orange), ab spiral (dark green), bc spiral (light green), the tilted $(a/c)b$ spiral (red), and the ac spiral (violet) phases. The coefficient, a, of the Landau expansion of the free energy (1) plays the role of temperature. Also plotted is the corresponding temperature dependence of the electric polarization, P_a (blue) and P_c (red) in zero field (b), $H_a = 0.5$ (c), $H_b = 0.3$ (e), and $H_b = 0.8$ (f). See Supplemental Material for details and the model parameters used in the calculation.

we keep only the most important terms. To describe effects of the magnetic rare-earth ions on the ordering of Mn spins we consider a strong temperature and field dependence of the anisotropy parameters, as discussed below. We then substitute $\mathbf{A} = (A_a, A_b, A_c)$ with $A_i = \Delta_i \cos(Qy + \varphi_i)$ $(i = a, b, c)$ into Eq. (1) and minimize f with respect to Δ_i and φ_i. The resulting phase diagrams for $H \parallel a$ and $H \parallel b$ together with the field dependence of the electric polarization are shown in Fig. 8.

At high temperatures rare-earth spins are disordered and the easy-axis anisotropy along the b direction present in manganites with both magnetic and nonmagnetic R ions favors the collinear incommensurate state, $A_b = \Delta_b \cos(Qy + \varphi_b)$ [brown color in Figs. 8(a) and 8(d)]. As temperature decreases and the modulation amplitude grows, the modulated A_a and A_c

orders appear. For close values of a_a and a_c, which is a special property of GDMO, we obtain the state with $\Delta_a, \Delta_c \neq 0$ and $\varphi_a = \varphi_c = \varphi_b \pm \frac{\pi}{2}$ (red color). This state, in which the ab and bc spirals coexist and have equal phases, is a tilted cycloidal spiral obtained, e.g., by rotating spins in the ab spiral around the b axis. In our calculation $a_a < a_c$, which gives rise to a narrow strip of the ab spiral phase between the collinear and tilted spiral phases.

As temperature decreases further, the coupling between the rare-earth and Mn subsystems induces the R order with the wave vector and symmetry of Mn spins, which in turn gives rise to an effective anisotropy of Mn spins with the Curie-like temperature dependence (see Supplemental Material for details [31]): $a_{a/c} = a_{a/c}^{(0)} - \frac{C_{a/c}}{T + \theta_{a/c}}$. The decrease of a_a and a_c with decreasing temperature ultimately turns the ac plane into

the magnetic easy plane, which triggers transition into the helical *ac* spiral state (violet color).

The polarization of the *R* spins by an applied magnetic field, *H,* leads to their partial decoupling from the Mn spins. This effect is described by an increase of the "Weiss constant," $\theta_{a/c}(H) = \theta_{a/c}(0) + \lambda C_{a/c} H^2$ (λ, $C_{a/c} > 0$), in the susceptibility of the rare-earth spins at the wave vector of the Mn spiral state, which affects the anisotropy parameters δa_a and δa_c and suppresses the *ac* spiral state (see Supplemental Material for details [31]). The difference in the effects of $H \parallel a$ (transition to the *bc* spiral state indicated by light green color) and $H \parallel b, c$ (reentrance into the tilted spiral state) results from different field dependence of a_a and a_c.

In conclusion, orthorhombic $Gd_{0.5}Dy_{0.5}MnO_3$ exhibits an electric polarization along a general direction in the *ac* plane which arises from the cycloidal spiral plane being rotated through $\sim 40°$ from the *ab* plane around the *b* axis. The cycloidal plane can be rotated by the application of an external magnetic field ($H \parallel a$) inducing a rotation of the polarization direction in the *ac* plane. This process occurs without symmetry breaking, contrary to the spin-flop transition reported in other known $R\text{MnO}_3$ compositions, and changes the P_a/P_c ratio by more than an order of magnitude. Magnetic fields applied along the *b* axis result in a monotonous increase of both P_a and P_c with an unusually strong effect: $P_a(8\,\text{T})$ at 2 K is 25 times larger than $P_a(0\,\text{T})$. The short-range rare-earth ordering suppresses the polar spiral ordering of Mn spins and gives rise to a largely helical state, not found in other rare-earth manganites, with a smaller electric polarization. Applied magnetic fields destroy the short-range ordering and lead to recovery of the cycloidal state.

[1] T. Kimura, T. Goto, H. Shintani, K. Ishizaka, T. Arima, and Y. Tokura, Nature (London) **426**, 55 (2003).

[2] T. Goto, T. Kimura, G. Lawes, A. P. Ramirez, and Y. Tokura, Phys. Rev. Lett. **92**, 257201 (2004).

[3] H. Béa, M. Gajek, M. Bibes, and A. Barthélémy, J. Phys.: Condens. Matter **20**, 434221 (2008).

[4] I. Kézsmárki, U. Nagel, S. Bordács, R. S. Fishman, J. H. Lee, H. T. Yi, S. W. Cheong, and T. Rõõm, Phys. Rev. Lett. **115**, 127203 (2015).

[5] S. Toyoda, N. Abe, S. Kimura, Y. H. Matsuda, T. Nomura, A. Ikeda, S. Takeyama, and T. Arima, Phys. Rev. Lett. **115**, 267207 (2015).

[6] N. A. Spaldin and M. Fiebig, Science **309**, 391 (2005).

[7] S.-W. Cheong and M. Mostovoy, Nat. Mater. **6**, 13 (2007).

[8] T. Kimura, Annu. Rev. Condens. Matter Phys. **3**, 93 (2012).

[9] Y. Tokura, S. Seki, and N. Nagaosa, Rep. Prog. Phys. **77**, 076501 (2014).

[10] M. M. Vopson, Crit. Rev. Solid State Mater. Sci. **40**, 223 (2015).

[11] T. Kimura, G. Lawes, T. Goto, Y. Tokura, and A. P. Ramirez, Phys. Rev. B **71**, 224425 (2005).

[12] K. Noda, S. Nakamura, J. Nagayama, and H. Kuwahara, J. Appl. Phys. **97**, 10C103 (2005).

[13] H. Katsura, N. Nagaosa, and A. V. Balatsky, Phys. Rev. Lett. **95**, 057205 (2005).

[14] M. Mostovoy, Phys. Rev. Lett. **96**, 067601 (2006).

[15] I. A. Sergienko and E. Dagotto, Phys. Rev. B **73**, 094434 (2006).

[16] J. Hemberger, F. Schrettle, A. Pimenov, P. Lunkenheimer, V. Y. Ivanov, A. A. Mukhin, A. M. Balbashov, and A. Loidl, Phys. Rev. B **75**, 035118 (2007).

[17] Y. Yamasaki, H. Sagayama, T. Goto, M. Matsuura, K. Hirota, T. Arima, and Y. Tokura, Phys. Rev. Lett. **98**, 147204 (2007).

[18] M. Mochizuki and N. Furukawa, Phys. Rev. B **80**, 134416 (2009).

[19] T. Goto, Y. Yamasaki, H. Watanabe, T. Kimura, and Y. Tokura, Phys. Rev. B **72**, 220403 (2005).

[20] T. Arima, T. Goto, Y. Yamasaki, S. Miyasaka, K. Ishii, M. Tsubota, T. Inami, Y. Murakami, and Y. Tokura, Phys. Rev. B **72**, 100102 (2005).

[21] N. Aliouane, O. Prokhnenko, R. Feyerherm, M. Mostovoy, J. Strempfer, K. Habicht, K. Rule, E. Dudzik, A. Wolter, and A. Maljuk, J. Phys.: Condens. Matter **20**, 434215 (2008).

[22] Y. Yamasaki, H. Sagayama, N. Abe, T. Arima, K. Sasai, M. Matsuura, K. Hirota, D. Okuyama, Y. Noda, and Y. Tokura, Phys. Rev. Lett. **101**, 097204 (2008).

[23] O. Prokhnenko, R. Feyerherm, E. Dudzik, S. Landsgesell, N. Aliouane, L. C. Chapon, and D. N. Argyriou, Phys. Rev. Lett. **98**, 057206 (2007).

[24] S. Ishiwata, Y. Kaneko, Y. Tokunaga, Y. Taguchi, T.-H. Arima, and Y. Tokura, Phys. Rev. B **81**, 100411 (2010).

[25] N. Zhang, S. Dong, Z. Fu, Z. Yan, F. Chang, and J. Liu, Sci. Rep. **4**, 6506 (2014).

[26] C. De and A. Sundaresan, App. Phys. Lett. **107**, 052902 (2015).

[27] L. C. Chapon, P. Manuel, P. G. Radaelli, C. Benson, L. Perrott, S. Ansell, N. J. Rhodes, D. Raspino, D. Duxbury, E. Spill, and J. Norris, Neutron News **22**, 22 (2011). The Neutron data for this work can be found at doi: 10.5286/ISIS.E.87839271.

[28] V. Petříček, M. Dušek, and L. Palatinus, Z. Kristallogr. - Cryst. Mater. **229**, 345 (2014).

[29] B. J. Campbell, H. T. Stokes, D. E. Tanner, and D. M. Hatch, J. Appl. Crystallogr. **39**, 607 (2006).

[30] C. De, S. Ghara, and A. Sundaresan, Solid State Commun. **205**, 61 (2015).

[31] See Supplemental Material at http://link.aps.org/supplemental/10.1103/PhysRevMaterials.3.044401 for details of magneti-

zation, dielectric, polarization, neutron-diffraction data, theory, and mcif files for each incommensurate structure. These files can be read with the free web application MVI-SUALIZE (http://webbdcrystal.ehu.es/magndata/mvisualize.php [J. M. Perez-Mato, S. V. Gallego, E. S. Tasci, L. Elcoro, G. d la Flor, and M. I. Aroyo, Annu. Rev. Mater. Res. (2015), 2045 :2013.2011–2013.2032]) that allows to visualize the structures in 3D and span the magnetic phases showing the rotation plane of the helical phases.

[32] N. Terada, Y. S. Glazkova, and A. A. Belik, Phys. Rev. B **93**, 155127 (2016).

[33] B. Koteswararao, K. Yoo, F. Chou, and K. H. Kim, APL Mater. **4**, 036101 (2016).

[34] S. Ghara, N. V. Ter-Oganessian, and A. Sundaresan, Phys. Rev. B **95**, 094404 (2017).

[35] R. D. Johnson, L. C. Chapon, D. D. Khalyavin, P. Manuel, P. G. Radaelli, and C. Martin, Phys. Rev. Lett. **108**, 067201 (2012).

[36] J. L. Ribeiro and L. G. Vieira, Phys. Rev. B **82**, 064410 (2010).